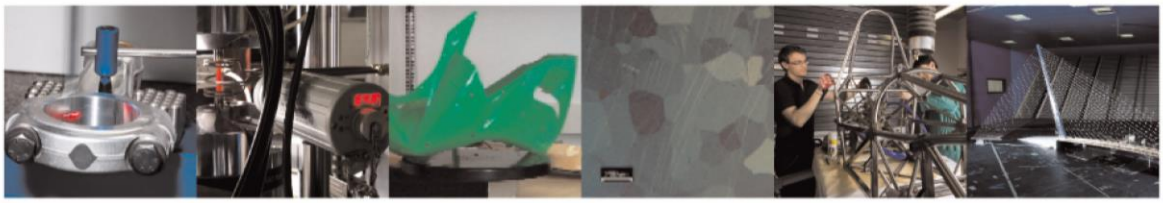

Complementary use of pulsed and continuous wave emission modes to stabilize melt pool geometry in laser powder bed fusion

Demir, Ali Gökhan; Mazzoleni, Luca; Caprio, Leonardo; Pacher, Matteo; Previtali, Barbara

This is a post-peer-review, pre-copyedit version of an article published in OPTICS AND LASER TECHNOLOGY. The final authenticated version is available online at:
http://dx.doi.org/10.1016/j.optlastec.2018.12.005

Complementary use of pulsed and continuous wave emission modes to stabilize melt pool geometry in laser powder bed fusion

Ali Gökhan Demir*, Luca Mazzoleni, Leonardo Caprio, Matteo Pacher, Barbara Previtali

Department of Mechanical Engineering, Politecnico di Milano, Via La Masa 1, 20156 Milan, Italy

*Corresponding author, aligokhan.demir@polimi.it

Complementary use of pulsed and continuous wave emission modes to stabilize melt pool geometry in laser powder bed fusion

Ali Gökhan Demir*, Luca Mazzoleni, Leonardo Caprio, Matteo Pacher, Barbara Previtali

Department of Mechanical Engineering, Politecnico di Milano, Via La Masa 1, 20156 Milan, Italy

*Corresponding author, aligokhan.demir@polimi.it

Abstract

The most common defects in laser powder bed fusion (LPBF) namely porosity, geometrical errors, roughness and thermal deformations are principally linked with the energy input to the process. In common practice, a single set of process parameters is used to produce a whole component independently from the dimensions of the actual scan path within a given layer. However, melt pool stability is highly dependent on the scanned geometry. A possible strategy to maintain a constant melt pool is the mixed use of pulsed wave (PW) and continuous wave (CW) emission regimes. Accordingly, this work investigates the complementary use of continuous and modulated emission at fixed energy density on large and thin sections respectively. The proposed approach is tested on AISI 316L stainless steel and melt pool observations are conducted employing a coaxial monitoring system built for purpose. Temporally resolved measurements of intensity and geometrical properties of the melt pool were extracted as well as a three-dimensional spatial mapping of the molten pool area. The results demonstrate that moving from CW to a PW regime at the transition zones to thinner sections is effective in maintaining a constant melt pool size thus avoiding heat build-up and part extrusion from the powder bed.

Keywords: Selective laser melting, molten pool monitoring, CW emission, PW emission, stainless steel.

1. Introduction

Laser powder bed fusion (LPBF) is an established industrial additive manufacturing process. The main challenges related to the process remain as material availability, lack of well-defined design rules and industrial standards, as well as process stability. The LPBF technology, in its full potential, is expected to produce complex, high value

components at first go [1]. However, the design and production phases still rely heavily on process experience. The end-users most commonly operate industrial systems with fixed parameter sets and processing conditions trying to achieve defect-free components. While, the design of the component itself and the use of support structures play an important role [2], the use of the same set of parameters for different geometries between different components and between different sections of the same component is an important limitation. Such limitation is highly related to the lack of knowledge about the consequences of process strategies for compensating or preventing process defects.

Most of the common defects in LPBF, such as porosity [3], geometrical deviations [4], thermal distortions [5], and delaminations [6] are related to the energy input. The energy input is most commonly managed by the laser parameters such as power and scan speed. The energy density is used to define the correct melting conditions, where lack-of-fusion is observed at low energy densities, and melt-pool instabilities are present with excessive energy densities [3]. An intermediate region exists, where most of the system manufacturers provide the process parameters for the supplied material. An important distinction between the commercial LPBF systems is the type of laser emission employed. While the majority of the industrial machines use continuous wave (CW) mode, pulsed wave (PW) emission through fast power modulation of the fiber laser source is applied by a smaller fraction of system providers [7]. Previous works have shown the relevance of using either mode for achieving higher melting capacity with CW or producing finer structures with PW [8–10]. The use of either mode is an intrinsic capability of contemporary fiber lasers. A critical point regards the place and timing of the intervention required on the distribution of the energy input. Fundamental studies regarding the differences in efficiency and precision due to different emission profiles provide results only by the end of the process [11,12]. Indeed, real time monitoring data is required to assess these differences and defect formation mechanisms[13,14].

The melt pool geometry is therefore an important indicator for depicting process stability in LPBF. A coaxial configuration can be more beneficial for determining the dimensions of the melt pool by following the laser beam at the processing zone [15]. Thermal cameras with correct emissivity calibration are highly promising for providing metrology data on the melt pool temperature [16][17]. However, their use in industrial LPBF systems in a coaxial

configuration is limited due to the reflectivity and transmissivity of the laser optics [18,19]. Use of pyrometry is also possible as this can also provide temperature measurements [20][21]. In this case, the temperature is an average of the observed zone and spatial resolution is lost. The use of photodiodes has the same limitation related to the spatial resolution, despite very fast temporal acquisition rates [22]. High speed cameras are also applied, yet the data burden can be excessive for monitoring applications [23]. The use of commercial digital cameras with reasonable responsivity in near infrared (NIR) region is a promising option [24]. Once opportunely calibrated with the correct thresholding value, the images can be used in a comparative manner to assess the melt pool geometry changes.

Accordingly, this work studies the effect of CW and PW emission modes on the melt pool geometry during the LPBF of AISI 316L. In particular, the effect of the emission modes is assessed on bulky and thin sections analysing the process changes due to the scanned geometry. For this purpose, an open LPBF platform has been used, where a custom made monitoring module was integrated. The monitoring module consisted in a commercial complementary metal–oxide–semiconductor (CMOS) camera with a band-pass filter collecting process thermal emission in the 850-1000 nm bandwidth. The measurements were calibrated via the images of the melt pool acquired using external illumination. A simple demonstrator geometry consisting of bulk and thin wall sections was produced using CW and PW emission at the same energy densities. Further, a mixed strategy was implemented assigning CW and PW emission to bulky and thin regions respectively. Three-dimensional melt pool maps were constructed from the monitoring data. The results show that the melt pool area can be kept more homogenous within and between layers by the use of the mixed emission strategy.

2. The mixed use of PW and CW emission modes

In CW emission mode the main process parameters are the laser power (P), scan speed (v) hatch distance (h) and layer thickness (z). When employing pulsed emission, on-the-fly modality is used, whereby the laser is scanned continuously over the scanned region and the laser power profile is modulated. Accordingly, the temporal and spatial distance between consecutive pulses can be further regulated. The pulse duration (t_{on}) is controlled through the power modulation signal. The spatial distance between the pulses is referred to as point distance (d_p). In

practical applications, the laser is commanded through a modulation signal with fixed pulse repetition rate (*PRR*) and duty (δ). For the sake of simple analogy, the pulse duration in CW can be accepted as infinite and the point distance as null. The energetic balance was maintained through the use of energy density parameter. For CW emission energy density F_{CW} is expressed as [25]:

$$F_{CW} = \frac{P}{h \cdot v_{CW} \cdot z} \tag{4}$$

where v_{CW} is explicitly the scan speed used for the CW emission. For PW emission energy density F_{PW} is expressed by substituting the CW power level with the average power of PW emission (P_{avg}) [26]:

$$F_{PW} = \frac{P_{peak} \cdot \delta}{h \cdot v_{PW} \cdot z} = \frac{P_{avg}}{h \cdot v_{PW} \cdot z} \tag{7}$$

The effect of emission mode requires to be evaluated in the same energetic conditions, thus at the same energy density. In order to assess the effect of emission mode over the scanned vector, the hatch distance and layer thickness should be the same. In order to address the differences in the temporal emission mode the same level of peak power at CW and PW emission should be kept, whilst exploiting fully the laser source output power (P=P_{peak}). Hence, the energetic conditions may be equalled by regulating the scan speed. As a result, a slower scanning speed is required with PW, in order to match the same level of energy density. For ideal square shaped pulses the scan speed in PW can be calculated as:

$$v_{PW} = v_{CW} \cdot \delta \tag{8}$$

However, the pulse shape may vary and deviate easily from the square shape in industrial lasers. Therefore, the correct scan speed should be set by measuring the average power at the desired pulse duration and duty using the following expression:

$$v_{PW} = v_{CW} \cdot \frac{P_{avg}(\delta)}{P} \tag{9}$$

3. Systems and materials

3.1 Open selective laser melting platform

A flexible prototype system for LPBF namely Powderful was used throughout this work [27]. The mechanical system consisted of a custom-made powder bed able to process small quantities of powder (<500 g), which was placed in a sealed chamber. Prior to processing an inertization procedure was carried out, where a cycle of vacuum down to -950 mbar and Ar purging up to 10 mbar was applied three times. The light source was a single mode fiber laser with 250 W maximum power (IPG Photonics YLR-150/750-QCW-AC, Cambridge, MA, USA). The laser beam was collimated with a 50 mm focal lens and launched into a zoom optic (VarioScan 20, Scanlab, Puchheim, Germany) to regulate the beam focal plane. Downstream the beam was manipulated and focused by the scanner head (HurryScan 14, Scanlab, Puchheim, Germany). The scanner housed a 420 mm f-theta lens. In this configuration, the beam diameter at the focal plane (d_0) was calculated as 60 µm. The control of the mechanical system and monitoring of the machine state were carried out in LabVIEW environment (National Instruments, Austin, TX) and the scan path trajectory was designed using SCANMASTER software (Cambridge Technologies, Bedford, MA). The open architecture allowed to modify process parameters down to the level of a single vector and the laser could be employed to emit both in CW and PW regime by power modulation.

Table 1. Main characteristics of the open LPBF platform Powderful.

Parameter	Value
Laser emission wavelength, λ	1070 nm
Max. laser power, P_{max}	250 W
Beam quality factor, M^2	1.1
Nominal beam diameter on focal plane, d_0	70 µm
Build platform area (DxWxH)	60x60x20 mm^3

3.2 Monitoring module

The coaxial monitoring module was implemented between the scan head and the focus optic working on a fixed image plane. A dichroic mirror transparent to the laser irradiation and reflective between 400-1000 nm was implemented. The monitoring module followed the f-theta lens, the galvanometric mirrors, the dichroic mirror down to a focusing system with an equivalent focusing distance of 120 mm. Between the focusing system and the

imaging sensor, different optical filters were implemented to capture the process emission at determined bands or the band of an illumination laser. A compact and industrial CMOS camera with adjustable pixel number and frame rate was installed as the sensor (Ximea xiQ USB Vision, Münster, Germany). The sensor size was 1280x1024 pixels, while pixel size was 4.8x4.8 μm^2. The optical system was configured to observe a field of view (FOV) of 4.3x4.3 mm^2 and 14 μm/pixel spatial resolution whilst the process images were acquired at 1200 fps.

The monitoring system was used with an external illuminator emitting at 640 nm (Cavitar, Cavilux HF, Tampere, Finland) synchronized with the camera. The illuminator was positioned at a lateral configuration with respect to the monitoring module. A short pass filter at 1000 nm was used to avoid back reflection of the process laser into the monitoring system (FSH1000, Thorlabs, Newton, NJ, USA). The actual melt pool geometry was observed with the reflected illumination light [28] using a band-pass filter at 650±10 nm (FB650-40, Thorlabs , Newton, NJ, USA). The molten pool geometry images were used to estimate the melt pool size.

Thermal emission images were acquired viewing the process emission in near infrared (NIR) region. Under the same conditions the process emission was observed between 850-1000 nm employing a long pass filter instead (FEL0850, Thorlabs, Newton, NJ, USA). Figure 1 depicts the configuration of the monitoring module.

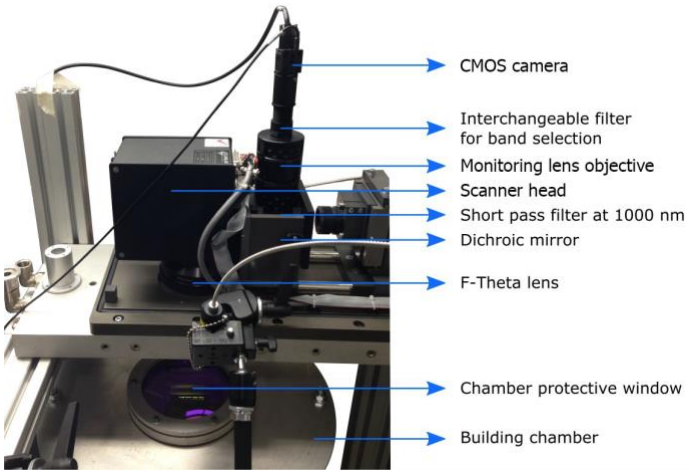

Figure 1. View of the LPBF system with monitoring module employed in this work.

3.3 Materials

Gas atomized AISI 316L stainless steel (Cogne Acciai, Brescia, Italy) powder was used in the present research. The apparent density is 4.07 g/cm3 whilst the powder size distribution was D10:23 µm, D50:32 µm, D90: 44 µm. The morphology and the particle size distribution are reported in Figure 2.

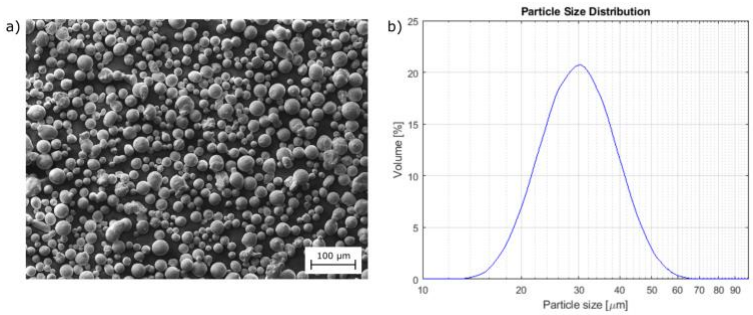

Figure 2. a) SEM image of AISI 316L powder. b) Powder size distribution.

3.4 Measurement of the melt pool dimensions

The system resolution was characterised prior to the measurements, assigning the pixel size to the images. The molten pool size is estimated performing static thresholding on thermal emission images of the molten pool, using a MATLAB routine. Thresholded images are binary matrices whose elements are 1 or 0 based on whether their original values were higher (or equal) or smaller than the threshold value. The threshold value was estimated by comparing thermal emission images with the real geometry of the molten pool acquired with external illumination (see Figure 3.a). The threshold constant (C) was set making the real area and the area computed with the procedure above match (see Figure 3.b). Finally, the value was fixed among images and the orientation of the molten pool did not affect the estimate. The ejected particles and spatters were isolated from the main melt pool. In these thresholded images, the molten pool appears as a white zone on a black background (see Figure 3.c). The effect of molten ejected particles is filtered out of these parameters thanks to a regions analysis: the molten pool "blob" is isolated from the others and parameters are therefore cleaned from disturbances (see Figure 3.c).

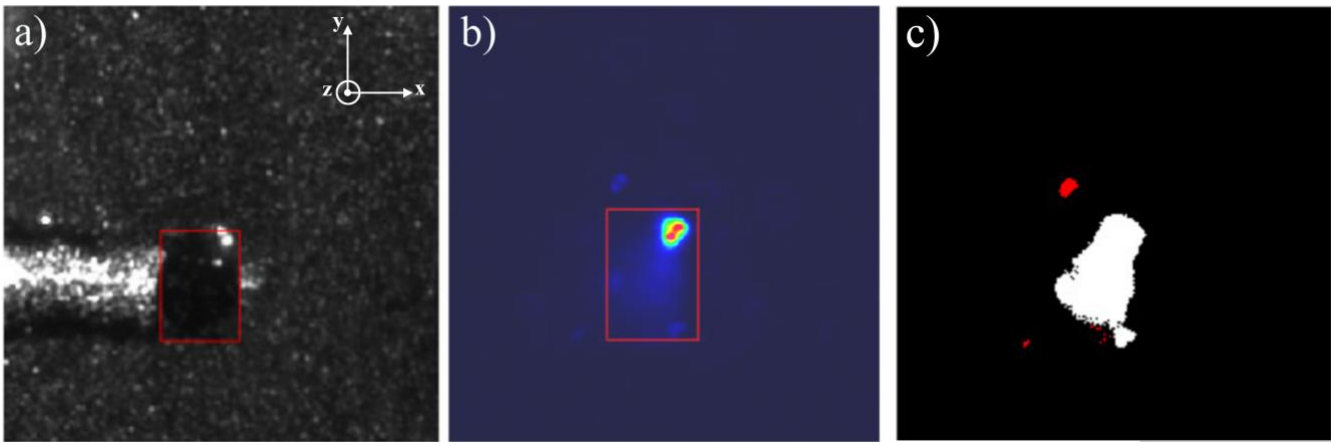

Figure 3. CW mode molten pool observations (x: hatching direction; y: scan direction; z: build direction). a) Real image acquired with the use of the external illumination system and b) thermal image in pseudocolors, where a threshold was set to make the two molten pools, whose extensions are indicated by red rectangles, have the same area. c) Thresholded image where the molten pool appears as a white blob and ejected particles are highlighted in red.

For each frame process indicators related to emission intensity and melt pool geometry were calculated. Before the application of the thresholding procedure, global frame intensity (I_k) was calculated on the raw thermal images as a sum of all pixel intensities using the following expression.

$$I_k = \sum_{i=1}^{m} \sum_{j=1}^{n} \tilde{p}_{k_{i,j}} \tag{10}$$

where k is the frame number, $p_{i,j}$ is the grey level of the pixel i,j and m,n are the pixel dimensions of the image(in this case m=n=304 pixels).

Melt pool length is defined as the maximum pixel count in melt pool thresholded zone parallel to the scan direction. In the application under analysis, the scanning direction is along the vertical direction of the frame, so the melt pool thermal emission length l_k for each frame k is calculated as the maximum thresholded pixel sum evaluated on every image column j:

$$l_k = \max\left(\sum_{i=1}^{m} \tilde{p}_{k_{i,j}}\right) r_s \tag{13}$$

where r_s is the spatial resolution and $\tilde{p}_{k_{i,j}}$ is the thresholded value of the pixel i,j of the image k according to the threshold constant C with the following the criteria.

$$\tilde{p}_{k_{i,j}} = \begin{cases} 1 \; if \; p_{k_{i,j}} \geq C \\ 0 \; else \end{cases} \tag{12}$$

Similarly, the melt pool width is considered as the maximum thresholed pixel sum evaluated on every image row i:

$$w_k = \max\left(\sum_{j=1}^{n} \tilde{p}_{k_{i,j}}\right) r_s \tag{14}$$

Melt pool area (A_k) was calculated after the threshold using the following expression

$$A_k = \sum_{i=1}^{m} \sum_{j=1}^{n} \tilde{p}_{k_{i,j}} \, r_s^2 \tag{11}$$

Due to the layerwise nature of the LPBF process, a process map for every layer can be created and stacked to compose a three-dimensional process status report, similar to a tomographic approach. One could expect to reconstruct the relative position of two consecutive frames by simply dividing the scanning speed and the frame acquisition rate, which are fixed parameters in the application under analysis. Nevertheless, the dynamic response of the optical scan system is not infinitely fast, and a transient time period is needed by the scanner system to reach the nominal scanning speed. This transient period where the scanner system accelerates to reach the stationary scanning velocity is present at the beginning of each scan line. In order to gather information on the actual position of a single acquisition frame, an image mapping algorithm is presented.

Since the powder bed is stationary, a relative displacement between two consecutive frames can be measured, representative of the real displacement induced by the laser scanning system when processing the powder bed. For the matching algorithm, external illumination is used in order to visualize the stationary powder bed, and the laser emission is not enabled in order to avoid process disturbances on the matching algorithm, thus obtaining a reliable position information. The relative displacement is measured by finding the maximum normalized cross-correlation between two consecutive acquired frames. The normalized cross-correlation (NCC) is defined as [29]:

$$\gamma(u,v) = \frac{\sum_{x,y}[f(x,y)-\bar{f}_{u,v}][t(x-u,y-v)-\bar{t}]}{\left\{\sum_{x,y}[f(x,y)-\bar{f}_{u,v}]^2 \sum_{x,y}[t(x-u,y-v)-\bar{t}]^2\right\}^{0.5}} \quad (15)$$

where f is the image, t is a $m\ x\ n$ subset, $\bar{t}$ is the mean of the subset, $\bar{f}_{u,v}$ is the mean of $f(x,y)$ in the region under the subset and $\gamma(u,v)$ is the normalized cross-correlation coefficient corresponding to horizontal and vertical displacements u and v of the searched subset t. The basic idea of NCC and cross-correlation in general is to set a search-area (subset) in the original image (frame i) and to find its new location in the following image (frame $i+1$). $\gamma_{x,y}$ has values in the range [-1,1] and its maximum value is reached when subset t in frame i and the corresponding region in frame $i+1$ are matched [29].

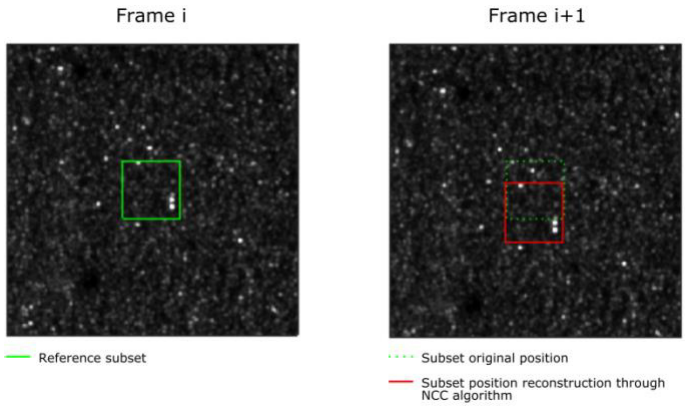

Figure 4. Measurement of relative displacement between two consecutive frames by finding the maximum NCC coefficient.

3.5 Experimental plan

A simple test geometry was adopted for the study that incorporated a bulk region (5x5 mm2) and two rectangular thin walls (10x1 mm2) as depicted in Figure 6. The scan direction was taken parallel to the shorter side of the thin walls. In particular, the effect of the emission regime on the melt pool area was investigated in the different regions as well as the transition zones for AISI 316L. Process parameters were set starting from CW regime, where the laser power was 200 W and scan speed 400 mm/s. The peak power in the PW emission was fixed at the same level, while a duty of 0.6 and pulse duration of 200 μs was selected. Figure 5 reports the temporal profile of the generated pulses. It can be seen that the pulse shape deviates from the ideal square shape with a ramped profile in the beginning and at the end. The peak power of the pulses is not modified significantly compared to the power level

in continuous wave. In these conditions, the average power in PW emission was measured as 108 W, thus the scan speed was fixed at 216 mm/s. For both regimes, the hatch distance and layer thickness were 70 µm and 50 µm respectively. For all the conditions, laser was focused on the powder bed and energy density was kept constant at 143 J/mm3. Both conditions were proved to produce fully dense components through preliminary experiments. Table 2 lists the parameters used with the two emission regimes.

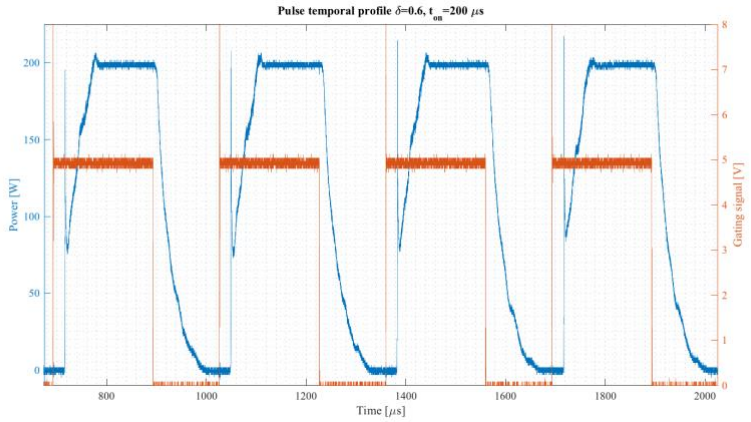

Figure 5. Temporal profile of the pulses used in the experiments .

Table 2. The set of parameters used in different emission regimes

Fixed parameters	CW	PW
Laser peak power, P_{peak} (W)	200	200
Laser average power, P_{avg} (W)	200	108
Duty, δ	1	0.6
Pulse duration, t_{on} (µs)	∞	200
Scan speed, v (mm/s)	400	216
Hatch distance, h (µm)	70	70
Point distance, d_p (µm)	0	72
Focal position, h_f (mm)	0	0
Layer thickness, z (µm)	50	50
Energy density, F (J/mm3)	143	143

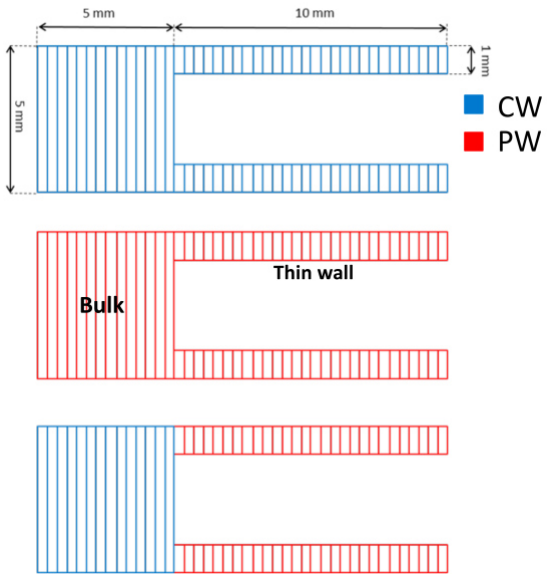

Figure 6. The employed geometry for testing the use of PW, CW, mixed emission modes.

The images were analysed qualitatively at an initial stage. Melt pool intensity, width, length, and area were extracted from the images. Melt pool area was assigned to scanned position to construct 3D maps in pseudo colour, evaluating the influence of emission regime on the scanned geometry.

4. Results

4.1 Image characteristics

Figure 7 reports thermal image in pseudocolors, which are representative of the different process conditions along the bulk and thin wall zones. Distinct melt pool geometries were observed under different emission regimes. Despite the same energy density is employed in CW and PW strategies, with PW emission the melt pool is observed to be smaller in area, shorter, and less intense in terms of emission. This improved melting efficiency of continuous wave emission has been previously shown, which is coherent with the observations [10]. On the other hand, moving towards the thin wall region, the melt pool geometry significantly changes. Larger dimensions and stronger process emission is observed overall for both CW and PW emission. In particular, with CW emission the melt pool width extends to several hatch lines, maintaining the melt pool over the whole width of the thin sections.

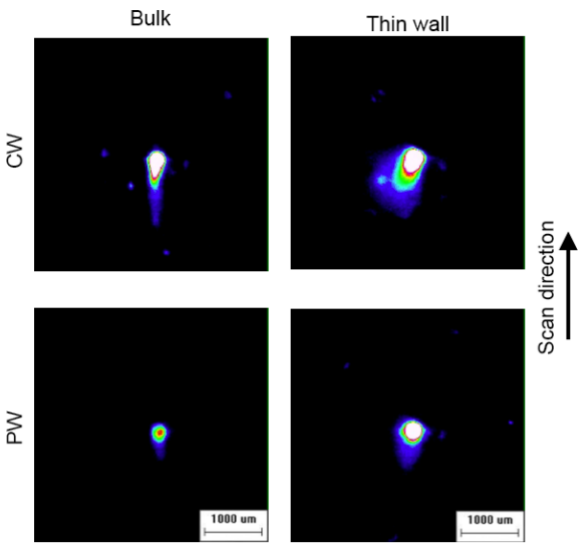

Figure 7. Melt pool thermal image in pseudocolors as a function of material, geometry, and emission profile.

4.2 Melt pool dimensions

4.2.1 Intensity and geometry with CW and PW emission

Figure 8 reports the length, width, and intensity measurements as a function of emission regime and position expressed as the scanned length (l) over the total length to be scanned (l_{tot}) at a single layer. The transition between bulk and thin section regions is approximately at l/l_{tot}=0.5. Amongst different process indicators, intensity appears to provide less significant results in terms of differences between the emission modes. A rise in intensity is visible between bulk and thin wall regions especially for CW emission. Such conditions are less remarked in PW emission. Due to these considerations, the use of a photodiode for resolving the differences between different geometrical regions and temporal emission modes seems to be limited. On the other hand, the width shows significant variations between the bulk and thin wall regions with the CW emission. The melt pool rises from approximately 0.7 mm towards 1.2 mm while changing the scan zone. The use of PW emission produces similar results, although in terms of magnitude the widths are smaller overall starting from around 0.4 mm in the bulk and rising to 0.6 mm in the thin wall section.

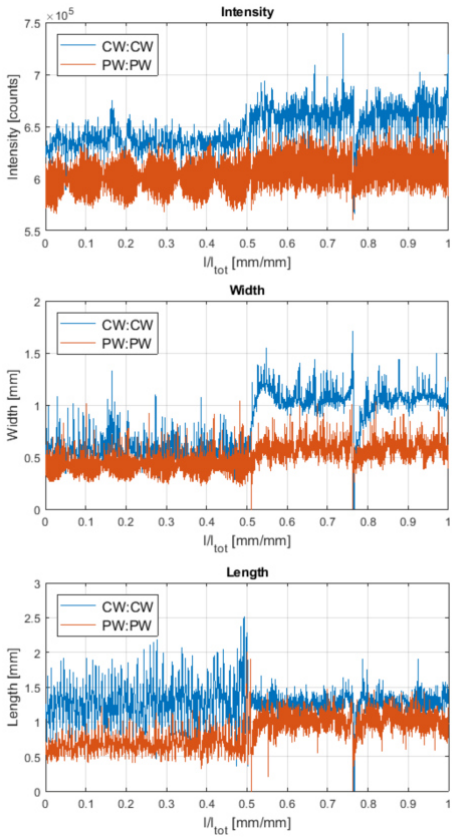

Figure 8. Melt pool length, width, and emission intensity as a function of scanned path length and emission type in a single layer.

With regards to the length measurements a strong cyclic behaviour was denoted in the bulk region. The minimum values for melt pool length are similar in CW and PW emission in the bulk region. On the other hand, melt pool length reaches values up to 2 mm with CW emission. A more stable behaviour is present in the thin wall region for both emission types. Apparently, the melt pool length exceeds the nominal size of the thin wall (1 mm) in CW emission reaching up to approximately 1.7 mm. A similar behaviour persists with PW emission, while the lengths are relatively smaller remaining around 1.2 mm.

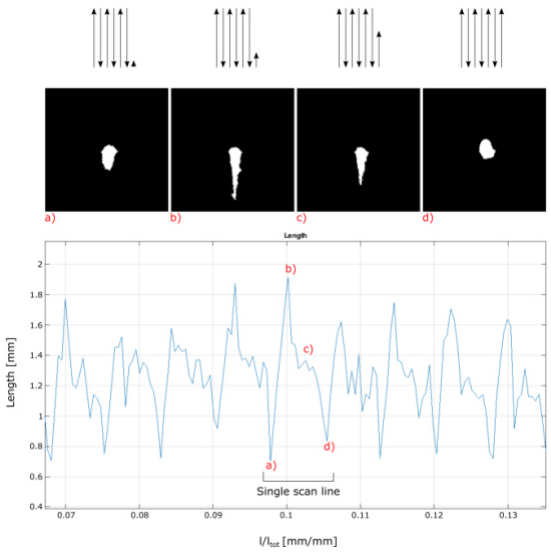

Figure 9. The cyclic behaviour of melt pool length shown at a) scan line beginning, b) acceleration phase, c) stable condition, d) scan line ending.

Figure 9 shows the cyclic behaviour of the melt pool length, specifically for CW emission. The dynamic response of the scan system for each single scan line results in a cyclic behaviour of melt pool length. When starting a new scan line, the melt pool features a short tail, but as soon as the scanner mirrors accelerate to reach the nominal speed, a peak in melt pool length is reached. Once the scanning reaches the defined scanning speed, the melt pool length stabilizes at an intermediate value up to the end of the scan line, where the deceleration phase implies a lower melt pool length. This cycle repeats for each scan line. The use of acceleration and deceleration strategies outside the scanned region can be beneficial. However, the heat accumulation due to the reduced scan lengths are expected to persist with constant energy input.

4.2.1 Intensity and geometry of mixed emission strategy

Figure 10 depicts the melt pool area as a function of different emission regimes, as well as showing the use of mixed emission strategy at a single layer. It can be noted that the melt pool area stands out as a more dynamic indicator in terms of the differences observed in the transition regions between bulk and thin wall zones. In particular, the melt pool area is approximately doubled in both CW and PW emissions as the process moves from the bulk region to the thin wall. With continuous wave emission, the melt pool area has an initial average value of

0.4 mm2, which then rises to 0.8 mm2. Similarly, the melt pool enlarges from 0.2 mm2 to around 0.4 mm2 in PW emission. The use of mixed emission mode compensates for such changes, proving a more homogenous melt pool area over the scanned layer.

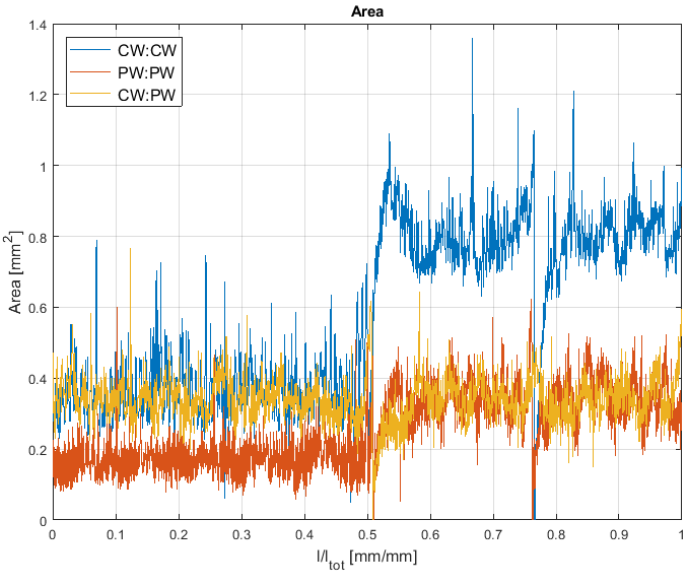

Figure 10. Melt pool area as a function of emission strategies showing the advantage of using mixed emission profile for stabilizing the melt pool area.

4.2.3 Molten pool area process maps

Further evaluation of melt pool area along with the position in the scanned part results in the 3D maps provided in Figure 11. The 3D maps indicate further details in the melt pool area evolution in the build direction. As expressed by the distribution of the colour maps the use of mixed emission provides a much smaller melt pool area variation over the workpiece. As seen in Figure 12, the acquired data provides pseudo-tomographic images, and can be used to view the melt pool distribution along different planes.

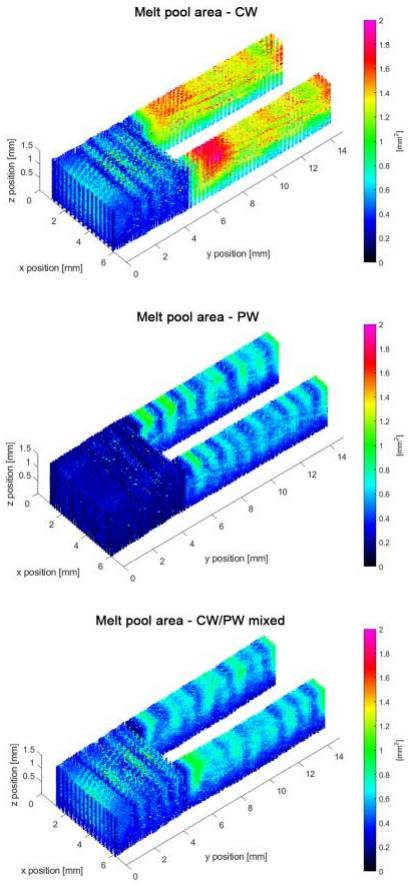

Figure 11. 3D spatial mapping of the melt pool area showing the interaction between the scanned geometry and the employed emission mode.

In CW emission, the heat accumulation plays a stronger role in the higher layers around the thin wall regions. With PW emission, the bulk region remains with smaller melt pool area significantly compared to the thin walls. The mixed emission provides a correct match between the melt pool areas of CW in the bulk zone and PW in the thin walls. Overall in all emission modes, the thin walls show a stabilizing behaviour after the initial layers. This is expected to be due to the formation of the stable layer thickness which depends on the powder size distribution and apparent density [30]. For the AISI 316L powder used in this work, considering the tap density and layer thickness values, the effective layer thickness reaches 75 µm at the second layer, and stabilizes at approximately 98 µm after the 8$_{th}$ layer. With higher effective layer thickness, laser emission can propagate further into the powder bed [31]. Combined with the overall temperature rise of the workpiece, the melt pool size is expected to increase throughout the initial layers. Krauss et al. [32] also demonstrated that around the proximity of the build plate,

thermal diffusivity is increased. A more effective heat dissipation implies a smaller melt pool. The same work underlines a reduced thermal dissipation around holes and overhang regions. In this work, the influence of scanned region size on reduced thermal dissipation is clearly demonstrated. In CW emission, an evident heat built up is present at the initial and final parts of the thin walls. This shows that the transition zones are more susceptible to defect formation.

The reason for melt pool enlargement in CW emission despite the use of higher scan speed shows that process efficiency is expected to change compared to PW emission. An important parameter for comparison purposes is the interaction time, which is the time required to travel the distance equal to the beam size for CW lasers, and the pulse duration for PW lasers [33]. Assuncao et al manipulated the interaction time with a CW laser by controlling the beam size weld speed with a fixed beam diameter [34]. They showed that with CW emission an increased interaction time results in higher weld penetration. The same group showed that the same interaction time results in higher weld penetration with PW emission compared to the CW due to the increase of the peak power [33]. In this work, the peak power of the PW emission and CW emission are kept constant. The interaction time of CW emission is calculated as 150 μs. Hence, it is shown that despite the use of a significantly slower scan speed and longer interaction time, the PW emission produces smaller melt pool. This phenomenon therefore cannot be explained merely by the interaction time. Previous work showed that PW emission with the same energy content generates significantly smaller melt tracks in LPBF [10]. This underlines the fact that overall process efficiency changes due to modulated power despite the use of the same energy. This can be used to maintain the melt pool size and avoid over heating as demonstrated in this work.

The vector length can be attributed to the heat accumulation and the thermal mass. Indeed, heat accumulation is already predominant in CW starting from the first layers, where the thermal mass is the whole build plate for both bulk and thin regions. In the thinner sections, the time required to overlap a given point is reduced as the scanned line is reduced. This corresponds to an overlap delay time, which means that the shorter the vector length the shorter the cooling time is. Hence, an overall increase of temperature is generated and the melt pool is enlarged. Further increase of the temperature generates the so called “hot spots” as reported in the literature [35]. Peak power

density is a comparison parameter provided in literature for the two types of emission modes. This parameter was demonstrated to be sufficient to explain the laser weld penetration for both emissions [33]. In this work, the peak power density was kept the same, while melt pool area effectively changes. Evidently the energy or power density functions are not able to fully describe the time dependant process behaviour.

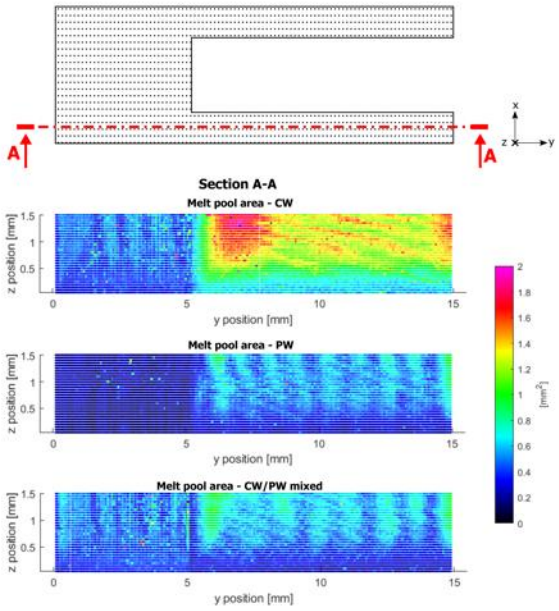

Figure 12. Pseudo-tomographic view of the melt pool area in a transversal cross-section taken along the zy plane passing from the centre of the thin wall.

The results provide several insights concerning the process dynamics and monitoring strategies. It can be seen that the equivalent energy inputs provide significant differences in terms of the melt pool size with different emission regimes. This indicates significant differences in the melting capacity of the different emission regimes. Caprio et al have shown empirically that the use of PW emission with the same energy content over single tracks result in significantly smaller melt track volume [36]. The melting behaviour observed with the multi-layered specimens in this work is coherent with the previous observations. Several mechanism may contribute to such differences, which lead to a difference in the process efficiency. It can be expected that the pulsed emission profile results in temporal temperature variations in the melt pool and the processing zone. Indeed, thermal capacity, density, and optical absorptivity are temperature dependant parameters. Especially the optical absorptivity increases in a non-linear

fashion for metals when molten phase is reached. A constant temperature profile can contribute to an increased process efficiency in these terms [37]. During the cyclic heating with PW emission, the laser beam is expected to hit a larger fraction of solid powder. As the optical absorption of the powder grains is less than that of the molten metal, the process efficiency may reduce. Another important factor to be considered is the angle of incidence that forms between the laser beam and the molten pool front. The incidence angle depends on the molten pool depth as well as the scan speed. The maximum optical absorption is achieved at Brewster angle. For molten iron, Brewster angle at 1 μm laser wavelength is approximately 80°. At lower scan speeds used with PW in order to compensate the energy input, the incidence angle can increase resulting in a drop of absorptivity [38]. The melt pool flow dynamics are expected to be significantly different for the two emission modes. The melt pool enlargement in CW mode can be also linked to the powder suction from the surrounding zones due to the melt and vapour flow around the processing zone [39]. This may lead up to denudation as well as part perturbations from the powder bed. Another important factor is related to the acceleration and deceleration zones in the scanned geometry. Working on a shorter scan track such as the case of the thin wall, the fraction of constant speed over the scanned track is reduced. In such circumstances, the possibility of keyhole formation may increase [40,41]. Hence, the melting capacity increases, along with the possibility of generating pores due to keyhole entrapment. For a better comprehension of the process dynamics, the information related to melt pool depth should be further assessed through complementary inline monitoring techniques.

From a practical perspective, it should be noted that the process parameters used in both regimes are able to provide fully dense components, whereas the management of the energy input becomes crucial for ensuring part quality. Geometrical accuracy relies also on the melt pool size for avoiding powder bed irregularities such as denudation, part extrusion, and delamination. The melt pool size also is strictly correlated to the cooling rates [42]. The generation of excessively large melt pools can lead to porosity formation, thermal distortions and cracking with more sensitive materials such as Al-, Ni-alloys and tool steels [23]. The use of fixed parameter sets along the whole component composed of variable sections is an apparent limitation to most of the industrial LPBF systems. A common practice is to manage the heat distribution through part orientation and the use of support structures. Such strategies can be limited to the part geometry. The use of support structures can become invasive as the post-

processing effort significantly increases [43]. Another approach is to use different scan strategies, tiling the larger sections to smaller ones as in the form of stripes, squares, or more complex fractal shapes [44]. While such strategy may be beneficial for larger sections, smaller sections can still suffer large heat accumulations resulting in hot spots [35]. Therefore, the possibility to assign the correct molten pool geometry and as a consequence emission strategy as a function of scan path is an option that requires further attention.

In terms of process monitoring, the use of a standard CMOS camera with sufficient sensitivity in NIR region provides several advantages. The results show that the spatial information is richer than what can be provided by intensity based measurements. Once opportunely calibrated, melt pool geometry can be analysed online. It should be noted that a strictly calibrated metrological instrument is not the main concern of the monitoring equipment required for the LPBF machines, whereas the process changes and drifts are required to be captured, allowing for a comparison based analysis. The thresholding applied was intended to capture the melt pool size, since it can be linked to most of the critical phenomenon related to defect formation occurring in the LPBF process. The use of such information is promising both for process control, as well as tailoring the heating and cooling cycles. Further efforts are required to resolve data flow and calculation burden in order to have such strategies applicable in real time.

5. Conclusions

In this work, the effect of PW and CW emission on the melting behaviour in LPBF is analysed using a coaxial monitoring module designed and implemented for the purpose. On an open LPBF platform, the melt pool geometry during the processing of AISI 316L stainless steel was observed in NIR region, compatibly with the industrial optics of a laser scanner and a high-performance, low-cost CMOS camera. The main conclusions of this work are as follows:

- The melt pool geometry relies highly on the temporal and spatial energy input. The energy and power density functions are not sufficient to describe the melting behaviour. In the experimented conditions the

same amount of energy density was applied with CW and PW emission regimes, which resulted in different melt pool extents.

- Camera based melt pool monitoring provides more dynamic signals compared to intensity based measurements. Once opportunely calibrated, the process indicators can be mapped in 3D, also providing pseudo-tomographic images of melt pool size distribution as a function of process parameters.
- The LPBF process parameters should be adapted to the scan geometry. Heat accumulation can occur at narrow sections, whereas larger sections can have melting deficiencies with the fixed parameters. The possibility to assign different emission types in different section of the build part is a promising solution for stabilizing the melt pool geometry.
- The use of melt pool size monitoring can be adapted to future control schemes. However, the process knowledge can be elaborated prior to the process in part planning for reducing defect formation probability. Process modelling is of aid for linking the duty cycle parameter to the scanned geometry, in particular to vector length.
- Thermal accumulations propagate also through different layers as the process proceeds. The use of melt pool size monitoring would be also adequate to observe slower thermal drifts between different layers. This can be beneficial for depicting thermal distortions

Another important point to be addressed for the process quality in LPBF is related to the defect correction. The use of mixed emission shows great promise for defect prevention and online process control schemes. However, in the event of defect formation, the monitoring device along with the position reconstruction algorithms can be used to employ remelting or ablation strategies before propagating to successive layers. Finally, further investigations are required to explain the differences between the use of PW and CW emission. The use of modelling techniques along with process monitoring is within future developments of the present study.

Acknowledgements

The authors gratefully acknowledge the collaboration of BLMGroup, IPG Photonics Italy, and Renishaw. This work was supported by European Union, Repubblica Italiana, Regione Lombardia and FESR for the project MADE4LO under the call "POR FESR 2014-2020 ASSE I - AZIONE I.1.B.1.3”.

References

[1] Weller C, Kleer R, Piller FT. Economic implications of 3D printing: Market structure models in light of additive manufacturing revisited. Int J Prod Econ 2015;164:43–56. doi:10.1016/j.ijpe.2015.02.020.

[2] Calignano F. Design optimization of supports for overhanging structures in aluminum and titanium alloys by selective laser melting. Mater Des 2014;64:203–13. doi:10.1016/j.matdes.2014.07.043.

[3] Gong H, Rafi K, Gu H, Starr T, Stucker B. Analysis of defect generation in Ti-6Al-4V parts made using powder bed fusion additive manufacturing processes. Addit Manuf 2014;1:87–98. doi:10.1016/j.addma.2014.08.002.

[4] Demir AG, Previtali B. Investigation of remelting and preheating in SLM of 18Ni300 maraging steel as corrective and preventive measures for porosity reduction. Int J Adv Manuf Technol 2017:1–13. doi:10.1007/s00170-017-0697-z.

[5] Zaeh MF, Branner G. Investigations on residual stresses and deformations in selective laser melting. Prod Eng 2010;4:35–45. doi:10.1007/s11740-009-0192-y.

[6] Harrison NJ, Todd I, Mumtaz K. Reduction of micro-cracking in nickel superalloys processed by Selective Laser Melting: A fundamental alloy design approach. Acta Mater 2015;94:59–68. doi:10.1016/j.actamat.2015.04.035.

[7] Demir AG, Colombo P, Previtali B. From pulsed to continuous wave emission in SLM with contemporary fiber laser sources: effect of temporal and spatial pulse overlap in part quality. Int J Adv Manuf Technol 2017;91. doi:10.1007/s00170-016-9948-7.

[8] Mumtaz KA, Hopkinson N. Selective Laser Melting of thin wall parts using pulse shaping. J Mater Process Technol 2010;210:279–87. doi:10.1016/j.jmatprotec.2009.09.011.

[9] Demir AG, Previtali B. Additive manufacturing of cardiovascular CoCr stents by selective laser melting. Mater Des 2017;119:338–50. doi:10.1016/j.matdes.2017.01.091.

[10] Caprio L, Demir AG, Previtali B. Comparative study between CW and PW emissions in selective laser melting. J Laser Appl 2018;30:032305. doi:10.2351/1.5040631.

[11] Demir AG, Previtali B. Investigation of remelting and preheating in SLM of 18Ni300 maraging steel as corrective and preventive measures for porosity reduction. Int J Adv Manuf Technol 2017;93. doi:10.1007/s00170-017-0697-z.

[12] Caprio L, Demir AG, Previtali B. Effect of pulsed and continuous wave emission on the densification behaviour in Selective Laser Melting. 39th Int Matador Conf 2017:1–7.

[13] Everton SK, Hirsch M, Stravroulakis P, Leach RK, Clare AT. Review of in-situ process monitoring and in-situ metrology for metal additive manufacturing. Mater Des 2016;95:431–45. doi:10.1016/j.matdes.2016.01.099.

[14] Grasso M, Colosimo BM. Process defects and *in situ* monitoring methods in metal powder bed fusion: a review. Meas Sci Technol 2017;28:044005. doi:10.1088/1361-6501/aa5c4f.

[15] Gökhan Demir A, De Giorgi C, Previtali B. Design and Implementation of a Multisensor Coaxial Monitoring System with Correction Strategies for Selective Laser Melting of a Maraging Steel. J Manuf Sci Eng Trans ASME 2018;140. doi:10.1115/1.4038568.

[16] Krauss H, Eschey C, Zaeh MF. Thermography for Monitoring the Selective Laser Melting Process. Proc. Solid Free. Fabr. Symp., 2012, p. 999–1014.

[17] Heigel JC, Lane BM. Measurement of the Melt Pool Length During Single Scan Tracks in a Commercial Laser Powder Bed Fusion Process. J Manuf Sci Eng 2018;140:051012. doi:10.1115/1.4037571.

[18] Criales LE, Arısoy YM, Lane B, Moylan S, Donmez A, Özel T. Laser powder bed fusion of nickel alloy 625: Experimental investigations of effects of process parameters on melt pool size and shape with spatter analysis. Int J Mach Tools Manuf 2017;121:22–36. doi:10.1016/j.ijmachtools.2017.03.004.

[19] Grasso M, Demir AG, Previtali B, Colosimo BM. In situ monitoring of selective laser melting of zinc

powder via infrared imaging of the process plume. Robot Comput Integr Manuf 2018;49. doi:10.1016/j.rcim.2017.07.001.

[20] Thombansen U, Gatej A, Pereira M. Process observation in fiber laser–based selective laser melting. Opt Eng 2014;54:11008. doi:10.1117/1.OE.54.1.011008.

[21] Furumoto T, Ueda T, Alkahari MR, Hosokawa A. Investigation of laser consolidation process for metal powder by two-color pyrometer and high-speed video camera. CIRP Ann - Manuf Technol 2013;62:223–6. doi:10.1016/j.cirp.2013.03.032.

[22] Craeghs T, Bechmann F, Berumen S, Kruth JP. Feedback control of Layerwise Laser Melting using optical sensors. Phys Procedia 2010;5:505–14. doi:10.1016/j.phpro.2010.08.078.

[23] Clijsters S, Craeghs T, Buls S, Kempen K, Kruth JP. In situ quality control of the selective laser melting process using a high-speed, real-time melt pool monitoring system. Int J Adv Manuf Technol 2014;75:1089–101. doi:10.1007/s00170-014-6214-8.

[24] Craeghs T, Clijsters S, Yasa E, Bechmann F, Berumen S, Kruth JP. Determination of geometrical factors in Layerwise Laser Melting using optical process monitoring. Opt Lasers Eng 2011;49:1440–6. doi:10.1016/j.optlaseng.2011.06.016.

[25] Thijs L, Verhaeghe F, Craeghs T, Humbeeck J Van, Kruth JP. A study of the microstructural evolution during selective laser melting of Ti-6Al-4V. Acta Mater 2010;58:3303–12. doi:10.1016/j.actamat.2010.02.004.

[26] Cherry JA, Davies HM, Mehmood S, Lavery NP, Brown SGR, Sienz J. Investigation into the effect of process parameters on microstructural and physical properties of 316L stainless steel parts by selective laser melting. Int J Adv Manuf Technol 2015;76:869–79. doi:10.1007/s00170-014-6297-2.

[27] Demir AG, Monguzzi L, Previtali B. Selective laser melting of pure Zn with high density for biodegradable implant manufacturing. Addit Manuf 2017;15. doi:10.1016/j.addma.2017.03.004.

[28] Kaierle S, Abels P, Kratzsch C. Process Monitoring and Control for Laser Materials Processing – An Overview. Proc. Lasers Manuf. 3, 2005, p. 101–5.

[29] Lewis JP. Fast Normalized Cross-Correlation. Vis Interface 1995;10:120–3. doi:10.1007/s00034-009-9130-7.

[30] Spierings AB, Levy G. Comparison of density of stainless steel 316L parts produced with selective laser melting using different powder grades. Proc. Solid Free. Fabr. Symp., 2009, p. 342–53.

[31] Mcvey RW, Melnychuk RM, Todd JA, Martukanitz RP. Absorption of laser irradiation in a porous powder layer. J Laser Appl 2007;19:214–24. doi:10.2351/1.2756854.

[32] Krauss H, Zeugner T, Zaeh MF. Thermographic process monitoring in powderbed based additive manufacturing 2015;177:177–83. doi:10.1063/1.4914608.

[33] Assuncao E, Williams S. Comparison of continuous wave and pulsed wave laser welding effects. Opt Lasers Eng 2013;51:674–80. doi:10.1016/j.optlaseng.2013.01.007.

[34] Assuncao E, Williams S, Yapp D. Interaction time and beam diameter effects on the conduction mode limit. Opt Lasers Eng 2012;50:823–8. doi:10.1016/j.optlaseng.2012.02.001.

[35] Grasso M, Laguzza V, Semeraro Q, Colosimo BM. In-Process Monitoring of Selective Laser Melting: Spatial Detection of Defects Via Image Data Analysis. J Manuf Sci Eng 2016;139:051001. doi:10.1115/1.4034715.

[36] Caprio L, Demir AG, Previtali B. Comparative study between CW and PW emissions in selective laser melting. 36th Int. Congr. Appl. Lasers Electro-Optics ICALEO, 2017, p. 1304.

[37] Steen WM, J. M. Laser Material Processing. vol. 1. 2010. doi:10.1007/978-1-84996-062-5.

[38] Mahrle A, Beyer E. Theoretical aspects of fibre laser cutting. J Phys D Appl Phys 2009;42. doi:10.1088/0022-3727/42/17/175507.

[39] Matthews MJ, Guss G, Khairallah SA, Rubenchik AM, Depond PJ, King WE. Denudation of metal powder layers in laser powder bed fusion processes. Acta Mater 2016;114:33–42. doi:10.1016/j.actamat.2016.05.017.

[40] King WE, Barth HD, Castillo VM, Gallegos GF, Gibbs JW, Hahn DE, et al. Observation of keyhole-mode laser melting in laser powder-bed fusion additive manufacturing. J Mater Process Technol 2014;214:2915–25. doi:10.1016/j.jmatprotec.2014.06.005.

[41] Khairallah SA, Anderson AT, Rubenchik A, King WE. Laser powder-bed fusion additive manufacturing: Physics of complex melt flow and formation mechanisms of pores, spatter, and denudation zones. Acta Mater 2016;108:36–45. doi:10.1016/j.actamat.2016.02.014.

[42] Yadroitsev I, Krakhmalev P, Yadroitsava I. Selective laser melting of Ti6Al4V alloy for biomedical applications: Temperature monitoring and microstructural evolution. J Alloys Compd 2014;583:404–9. doi:10.1016/j.jallcom.2013.08.183.

[43] Lefky CS, Zucker B, Wright D, Nassar AR, Simpson TW, Hildreth OJ. Dissolvable Supports in Powder Bed Fusion-Printed Stainless Steel. 3D Print Addit Manuf 2017;4:3–11. doi:10.1089/3dp.2016.0043.

[44] Catchpole-Smith S, Aboulkhair N, Parry L, Tuck C, Ashcroft IA, Clare A. Fractal scan strategies for selective laser melting of 'unweldable' nickel superalloys. Addit Manuf 2017;15:113–22. doi:10.1016/j.addma.2017.02.002.

List of tables

List of figures